Nano Energy 78 (2020) 105197

Contents lists available at ScienceDirect

Nano Energy

journal homepage: http://www.elsevier.com/locate/nanoen

Semimetallic features in thermoelectric transport properties of 2H–3R phase niobium diselenide

Hongjae Moon [a,1], Jeongmin Kim [b,1], Joonho Bang [c], Seokkyoon Hong [a], Seonhye Youn [a], Hyunjun Shin [a], Jong Wook Roh [d], Wooyoung Shim [a], Wooyoung Lee [a,*]

[a] Department of Materials Science and Engineering, Yonsei University, 50 Yonsei-ro, Seodaemoon-gu, Seoul, 03722, South Korea
[b] Division of Nanotechnology, DGIST, 333 Techno Jungang-daero, Hyeonpung-eup, Dalseong-gun, Daegu, 42988, South Korea
[c] Department of Energy Science, Sungkyunkwan University, Suwon, 16419, South Korea
[d] School of Nano & Materials Science and Engineering, Kyungpook National University, Gyeongsangbuk-do, 37224, South Korea

ARTICLE INFO

Keywords:
Polymorph
Niobium diselenide
Electrical conductivity
Seebeck coefficient
Thermoelectricity
Energy harvesting

ABSTRACT

In two-dimensional van der Waals crystals, the interlayer stacking sequence often leads to a change in crystal symmetry and, thus, new polymorphs, leading to an abundant array of physical properties. In this paper, we report the polymorphic form of 2H–3R–$NbSe_2$ that exhibits a substantial difference in terms of the gate dependence of semimetallic behavior and Seebeck coefficient, compared to the well-known 2H–$NbSe_2$ with metallic transport behavior. The semimetallic features of 2H–3R–$NbSe_2$ indicate the presence of minor carriers, confirmed through theoretical calculations, which is in good agreement with the transport behavior. Our results reveal perspectives for understanding the metastable 2H–3R phase $NbSe_2$, which is not far from equilibrium, and for engineering the materials necessary for efficient energy harvesting.

1. Introduction

Two-dimensional (2D)-layered materials provide opportunities to explore largely unreached areas of the materials space. Generally, the physical properties of layered materials are considerably different from those of bulk materials, providing a greater degree of freedom for potential applications. This difference, compared to bulk materials, is primarily caused by the weak van der Waals (vdW) bonds that hold two adjacent layers together. Consequently, the search for new 2D material candidates has been accelerated to expand the array of prospective vdW-bonded materials [1,2]. High-throughput computational methods fall into this category and represent a powerful tool for exploring the material space beyond semiconductors (e.g., MoS_2) [3], insulators (e.g., hexagonal boron nitride) [4], and semimetals (e.g., graphene), providing a guideline to synthetic routes for producing 2D materials with a variety of material properties [5].

Owing to the insufficient strength in vdW bonds, various interlayer stacking sequences can exist, and, consequently, modulating the stacking order is another pathway to customize the physical properties of 2D materials [6]. The semiconducting polymorphs 2H–MoS_2 and 3R–MoS_2 are good examples of a case where the stacking can determine the crystal symmetry. A bilayer 2H–MoS_2 possesses an inversion center [7], while 3R–MoS_2 is noncentrosymmetric [8], leading to various valleytronic [9] and ferroelectric characteristics [10]. For example, graphene trilayers with ABA (bernal) and ABC (rhombohedral) stacking exhibit significantly different electronic band dispersions that affect many physical properties, such as infrared absorption [11], band gap energy [12], and quantum Hall transport [13,14]. For the twisted modulation of graphene [15], the resulting Moire superlattice structures can exhibit various exotic phenomena, such as fractional quantum Hall effects [16] and Van Hove singularities [17]. Therefore, efforts have been focused on searching for metastable 2D crystalline materials wherein the stacking sequence enables property differentiation at the device level. To date, only few studies have explored beyond graphene and MoS_2 and toward the materials space.

In this paper, we report the first polymorphic form of 2D $NbSe_2$ with the polytypic disorder of semimetallic 2H–3R–$NbSe_2$, compared to the well-known metallic 2H–$NbSe_2$ with superconductivity [18]. The metastable state of the polymorph 2H–3R–$NbSe_2$ was demonstrated by total energy calculations. To examine the band engineering based on the

* Corresponding author.
E-mail address: wooyoung@yonsei.ac.kr (W. Lee).
[1] H. Moon and J. Kim contributed equally to this work.

https://doi.org/10.1016/j.nanoen.2020.105197
Received 22 May 2020; Received in revised form 9 July 2020; Accepted 12 July 2020
Available online 31 July 2020

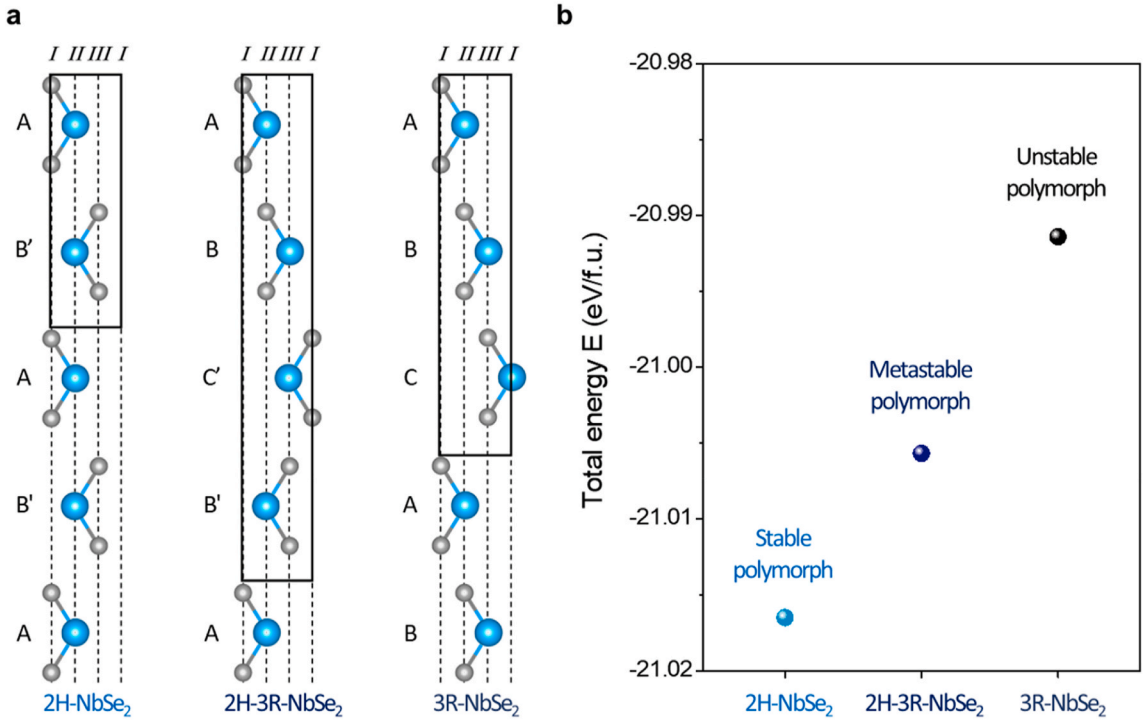

Fig. 1. Stacking types and thermodynamic stabilities of $NbSe_2$ phases. (a) Schematic of stacking sequences of 2H–$NbSe_2$, 2H–3R–$NbSe_2$, and 3R–$NbSe_2$. The large blue and small grey circles represent the Nb and Se atoms, respectively. In the honeycomb lattice, three atomic coordinates are on the basal plane: I: 0, 0; II: 1/3, 2/3; III: 2/3, 1/3. (b) Calculated total energy of the 2H, 2H–3R, and 3R phase $NbSe_2$.

polymorph formation, we systematically investigated the thermoelectric transport properties of 2H–$NbSe_2$ and 2H–3R–$NbSe_2$. The semimetallic 2H–3R–$NbSe_2$ shows a substantial difference in gate dependence of conductance and Seebeck coefficient, indicating the presence of minor carriers that have not been observed in the metallic 2H–$NbSe_2$. Further, the theoretically obtained band structures elucidate the different electrical transport behaviors in the two phases. The results demonstrate that the semimetallic 2D $NbSe_2$ is a promising platform to explore polytypic disorder and its effects on related properties that are extremely sensitive to the band structure and asymmetry of electrons and holes, such as thermoelectricity.

2. Experimental section

2.1. Material synthesis and characterizations

2H–3R–$NbSe_2$ phase bulk crystals were synthesized using a solid-state reaction method. The niobium powder (<45 μm, 99.8%, Sigma-Aldrich) and selenium powder (100 mesh, 99.99%, Sigma-Aldrich) were mixed with a molar ratio of 1:2. The mixture, in anhydrous ethanol, was ball-milled (Planetary Mill, Fritsch) at 300 rpm for 24 h. The ball-milled mixture was then dried at 90 °C for 12 h using a vacuum oven. The as-prepared mixture was sealed in an evacuated quartz tube and annealed at 1050 °C for 72 h.

X-ray diffraction (XRD, Ultima IV/ME 200DX, Rigaku) was used for the phase analysis of each crystal powder. The layered crystal structures of the exfoliated 2H- and 2H–3R-layered $NbSe_2$ were characterized using Raman spectroscopy (LabRam ARAMIS, Horiba Scientific), X-ray photoelectron spectroscopy (K-alpha, Thermo Fisher Scientific, Inc.), atomic force microscopy (AFM, XE-150, Park Systems), Cs-corrected scanning transmission electron microscopy (STEM, JEM-ARM 200F, Jeol), and dual beam focused ion beam (FIB, crossbeam 540, ZEISS).

2.2. Device fabrication and measurements

Layered $NbSe_2$ was obtained by mechanical exfoliation from 2H (HQ graphene) and 2H–3R phase bulk crystals onto a highly doped p-type Si substrate with a thermally grown SiO_2 layer (thickness of 300 nm) on top. The electron-beam lithography (VEGA3, Tescan and NPGS, JC Nabity Lithography Systems) was performed to generate patterns on the dispersed layered $NbSe_2$ for transport measurements. Prior to the metallization of Ti (5 nm)/Au (100 nm) electrodes using an ultra-high vacuum sputtering system, the patterned layered $NbSe_2$ was exposed to Ar plasma for 15 s to enhance the electrical contact between the layered $NbSe_2$ and the electrodes.

The transport properties of layered $NbSe_2$ were measured by a micro device, which comprises a heater electrode and two thermometers. Electrical conductivity was obtained using an *I–V* measurement system (2182, Keithley). To measure the thermopower, the voltage difference and temperature gradient between the two thermometers were generated by Joule heating of the heater electrode. The voltage difference was measured using a nano-voltmeter (2182, Keithley), and the temperature gradient was measured from the temperature coefficient of the resistance of each thermometer by obtaining the thermometer resistance using a lock-in amplifier (SR850, Stanford Research Systems). All measurements, including gate- and temperature-dependent properties, were performed using a cryostat system (X-1AL, Advanced Research Systems) in a high vacuum.

2.3. Band structure and total energy calculations

First-principle density functional theory (DFT) calculations were performed using the generalized gradient approximation (GGA) with the Perder–Burke–Ernzerhof functional and the projector augmented plane-wave method implemented in the Vienna *ab initio* simulation program code [19–21]. The 4p, 4d, and 5s electrons of Nb and the 4s and 4p electrons of Se were used as valence electrons. The plane-wave basis cut-off energy was set to 600 eV. A vdW correction was included using

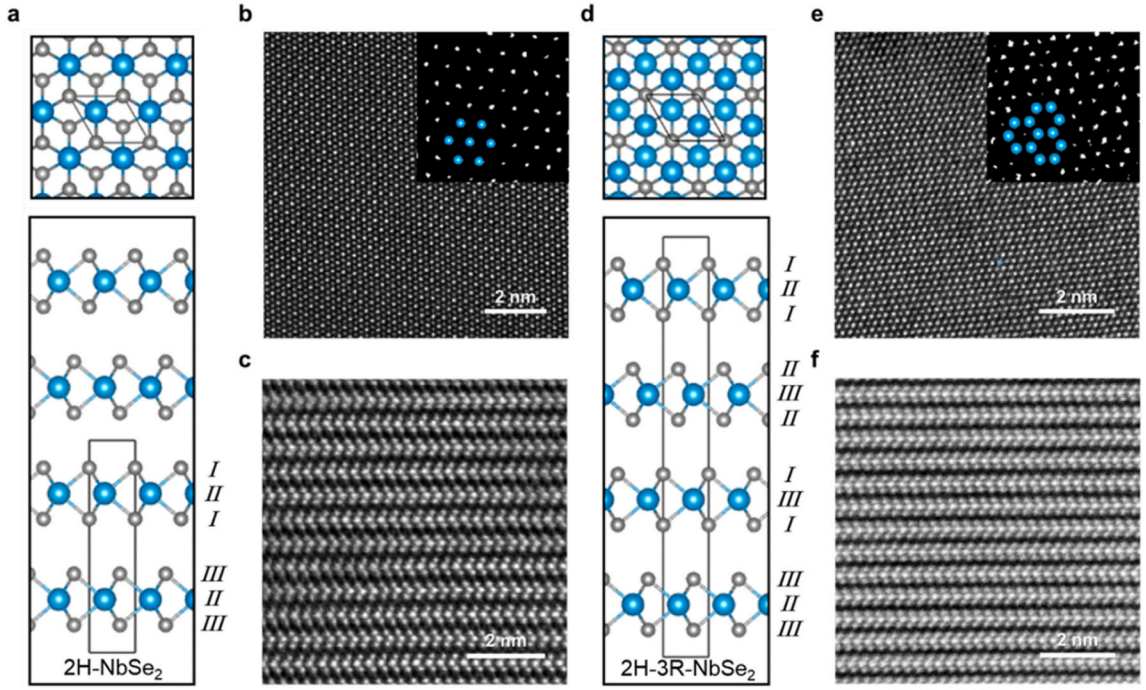

Fig. 2. Structural characterization of the 2H and 2H–3R phase $NbSe_2$. (a, d) Top view and side view of stick-and-ball lattice structures of layered $NbSe_2$ with typical 2H (a) and 2H–3R (d) phases. (b, e) HR-STEM images of mechanically exfoliated $NbSe_2$ with typical 2H (b) and 2H–3R (e) phases. The insets are the Nb atom arrays obtained by contrast adjustment. The magnification is twice that of the original STEM image. (c, f) Cross-sectional HR-STEM images of vertically sliced $NbSe_2$ with typical 2H (c) and 2H–3R (f) phases.

the DFT-D3 method with Becke–Johnson rational damping, and [22,23] k-point meshes of 12 × 12 × 3, 12 × 12 × 2, and 12 × 12 × 2 were used for the 2H, 2H–3R and 3R structures, respectively. Further, structural relaxation was performed until the Hellmann-Feynman forces were less than 1×10^{-5} eV $Å^{-1}$.

3. Results and discussion

3.1. Metastable polymorph of $NbSe_2$

The three polymorphs of $NbSe_2$, namely, 2H, 3R, and 2H–3R, have trigonal prismatic coordination of the Nb atoms, but with different stacking sequences (Fig. 1a). In 2H–$NbSe_2$, the Nb atoms of each layer are located on the same atomic coordinate (II), and the Se atoms are on two different coordinates (I and III) for each layer. Conversely, 3R–$NbSe_2$ consists of three staggered layers, where the Nb atoms are on different coordinates (I, II, and III) for each layer. Therefore, the Se atoms of one layer are situated above the Nb atoms of a lower adjacent layer. In contrast, 2H–3R–$NbSe_2$ has a more complex stacking order with the 2H and 3R structures combined. The unit cell of 2H–3R–$NbSe_2$ consists of four layers of $NbSe_2$, stacked by repeating the 2H and 3R stacking order. Consequently, Nb and Se atoms of different layers are located above and below the Nb atoms of a layer, respectively.

To evaluate the thermodynamic stabilities of the $NbSe_2$ polymorphs, the total energy per formula unit (f.u.) of each phase was calculated using a GGA (Fig. 1b) [21]. The total energy of 2H–$NbSe_2$ has the lowest value among the three polymorphs, indicating that the 2H stacking sequence is the most stable structure. For 3R–$NbSe_2$, the calculated total energy is 25 meV higher than that of 2H–$NbSe_2$, indicating that it is the most unstable structure. For 2H–3R–$NbSe_2$, the total energy is slightly higher (11 meV) than that of 2H–$NbSe_2$ and lower (14 meV) than that of 3R–$NbSe_2$, implying that it is the metastable structure among the three polymorphs.

3.2. Structural characterization

To confirm the stacking pattern of the atomic layers, the atomic structure of the 2H–$NbSe_2$ and 2H–3R–$NbSe_2$ was characterized via high-resolution STEM (HR-STEM) (Fig. 2). A single layer in 2H–$NbSe_2$ comprises three atomic sublayers with an Nb layer sandwiched between two Se layers (Fig. 2a) [24]. Although each Nb atom is actually bonded to six Se atoms with a trigonal prismatic geometry, only three Se atoms surrounding the Nb atom can be observed in the single-layer top view image [25]. Therefore, the top-view STEM image of 2H–$NbSe_2$, which shows Nb atoms surrounded by six Se atoms, indicates the AB′ double-layer stacking order (Fig. 2b). To observe the stacking pattern directly, we prepared a vertically sliced specimen, and the cross-sectional STEM image clearly shows the AB' stacking of the 2H–$NbSe_2$ phase (Fig. 2c). The lattice constants were found to be a = 0.35 nm and c = 1.26 nm from the spacings of the (100) and (001) planes, respectively, which are in good agreement with a previous study [26].

Conversely, the 2H–3R phase has quadruple layers of $NbSe_2$ with the ABC'B' stacking order, with 2H AB′(BC′) and 3R AB(C'B') stackings combined. While each Nb atom in one layer eclipsed an Nb atom in the other layer for the 2H double layers, the stacking in the 3R double layers is shifted, with an Nb atom in one layer over an Se atom in the other layer (Fig. 2d). Therefore, in the top-view STEM image of 2H–3R–$NbSe_2$, six Nb atoms can be observed surrounding one Se atom (Fig. 2e). The honeycomb array of Nb atoms is obtained by removing the dark Se spots using a contrast adjustment of the 2H–3R–$NbSe_2$ STEM image, and it clearly shows the difference in the stacking order from the 2H–$NbSe_2$ (insets of Fig. 2b and e). Using a vertically sliced specimen, the ABC'B' stacking of the 2H–3R–$NbSe_2$ phase was directly confirmed by the cross-sectional STEM image (Fig. 2f). Moreover, the interatomic and interlayer spacings and y–z plane atomic arrangement of the 2H–3R–$NbSe_2$ phase were found to be almost the same as those of 2H–$NbSe_2$ phase (Fig. S1).

The crystal structures of the 2H–$NbSe_2$ and 2H–3R–$NbSe_2$ powders

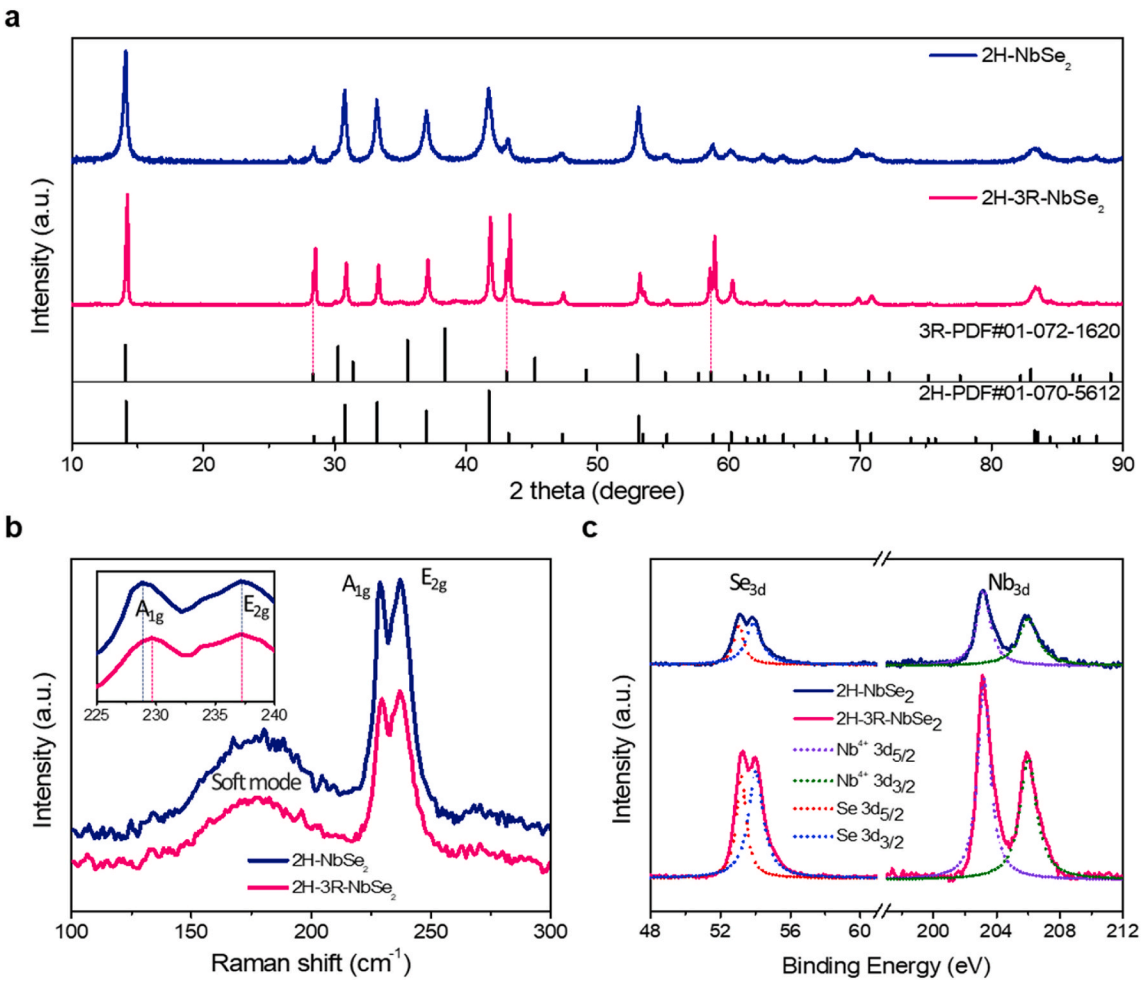

Fig. 3. XRD, Raman, and XPS data of 2H–$NbSe_2$ and 2H–3R–$NbSe_2$. (a) XRD patterns of 2H- and 2H–3R–$NbSe_2$ crystal powders. (b) Raman spectra of layered 2H–$NbSe_2$ and 2H–3R–$NbSe_2$. (c) XPS spectra of layered 2H–$NbSe_2$ and 2H–3R–$NbSe_2$.

were characterized through XRD analysis (Fig. 3a). The diffraction patterns of the 2H–$NbSe_2$ matched well with the reference diffraction data of hexagonal 2H–$NbSe_2$ (PDF # 01-070-5612; space group: $P6_3/mmc$). However, owing to the mixed stacking sequence, additional peaks near the 28.4°, 43.1°, and 58.6° were observed in the diffraction patterns of 2H–3R–$NbSe_2$, which originated from the (006), (009), and (0012) planes of trigonal 3R–$NbSe_2$ (PDF # 01-072-1620; space group: $R3m$).

We performed Raman spectroscopy of few-layered 2H–$NbSe_2$ and 2H–3R–$NbSe_2$ to confirm the layered structure of $NbSe_2$. We observed two sharp peaks in 2H–$NbSe_2$ near 228 and 237 cm^{-1}, corresponding to the A_{1g} and E_{2g} Raman active modes (Fig. 3b). These results are in good agreement with those in a previous study on 2H–$NbSe_2$ crystals synthesized by the vapor transport method [27]. For 2H–3R–$NbSe_2$, the out-of-plane vibration A_{1g} mode blue shifts slightly (~1 cm^{-1}), while the in-plane vibration E_{2g} mode remains unchanged, compared to those of 2H–$NbSe_2$. This Raman peak shift originates from the stacking difference between two samples; this finding is in good agreement with that of the previous study on stacking-dependent Raman spectra [28]. The broad peak centered at 180 cm^{-1} is a soft mode peak, which originated from the second-order scattering of two phonons [18].

The chemical states of layered 2H–$NbSe_2$ and 2H–3R–$NbSe_2$ were examined by X-ray photoemission spectroscopy (XPS) (Fig. 3c). The peaks at 203.1 and 205.8 eV and 203.1 and 205.9 eV can be assigned to Nb^{4+} $3d_{5/2}$ and Nb^{4+} $3d_{3/2}$ of 2H–$NbSe_2$ and 2H–3R–$NbSe_2$, respectively. Meanwhile, the peaks at 53.1 and 53.8 eV and 53.3 and 54.0 eV can be assigned to Se $3d_{5/2}$ and Se $3d_{3/2}$ of 2H–$NbSe_2$ and 2H–3R–$NbSe_2$, respectively. These results are well aligned with the corresponding binding energies of Nb and Se reported for CVD-grown few-layer $NbSe_2$ sheets and bulk $NbSe_2$ [25,29]. According to the XPS measurements, the two different structures of the $NbSe_2$ samples (e.g., 2H–$NbSe_2$ and 2H–3R–$NbSe_2$) are assumed to have a small effect on the overall chemical states of $NbSe_2$. The absence of Nb^{5+} $3d_{5/2}$ and Nb^{5+} $3d_{3/2}$ peaks at higher binding energy, from 207.3 to 211.0 eV, implies that niobium oxide Nb_2O_5 was not produced during or after fabrication processes [30]. Low-magnification TEM and EDS images also confirm the chemical composition of the 2H–3R phase $NbSe_2$ (Fig. S2).

3.3. Transport characterization

To verify the change in transport phenomena caused by the different stacking patterns between 2H–$NbSe_2$ and 2H–3R–$NbSe_2$, we investigated the electrical conductivity and Seebeck coefficient of both samples (Fig. 4). The thermoelectric transport properties are quite sensitive to the intrinsic properties, such as carrier density and mobility. In particular, the Seebeck coefficient becomes more sensitive to the carrier density when minor carriers are present owing to the opposite signs of partial Seebeck coefficients in electron and hole [31,32]. Therefore, a change in the band structures can be easily examined based on the thermoelectric transport properties.

Based on our DFT calculations and previous studies on transition metal dichalcogenide nanosheets, mechanically exfoliated $NbSe_2$ flakes with a thickness of less than 10 nm were selected for transport measurements to provide sufficient back gate field effect to examine the

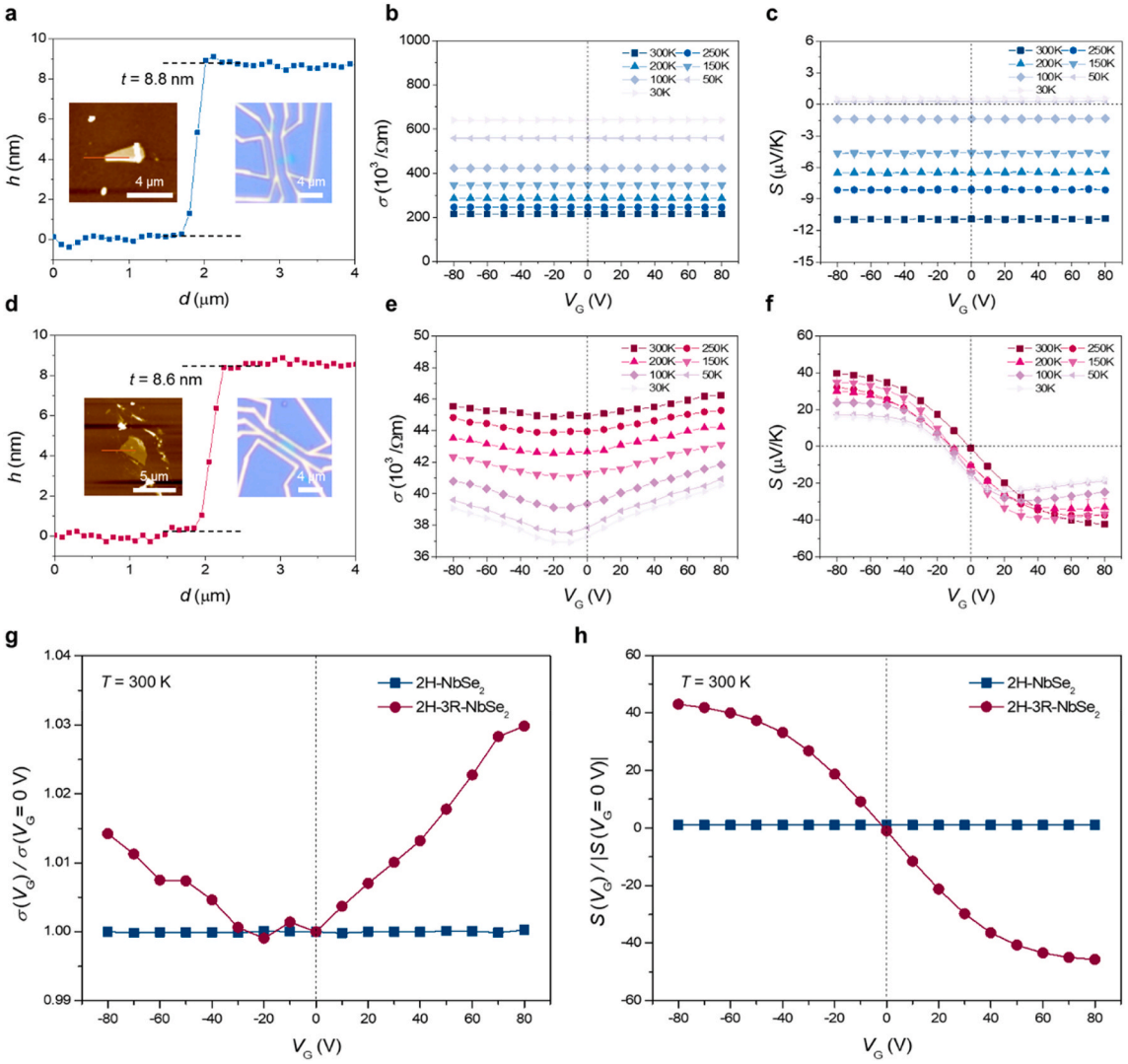

Fig. 4. Transport characterization. AFM profiles of layered (a) 2H–$NbSe_2$ and (d) 2H–3R–$NbSe_2$. The topographic AFM image of mechanically exfoliated $NbSe_2$ (left inset) and optical microscopy image of fabricated micro-devices (right inset). (b, e) Temperature- and gate-dependent electrical conductivity of layered (b) 2H–$NbSe_2$ and (e) 2H–3R $NbSe_2$ from 300 to 30 K. (c, f) Temperature- and gate-dependent Seebeck coefficient of layered (c) 2H–$NbSe_2$ and (f) 2H–3R from 300 to 30 K. (g, h) Gate-dependent normalized electrical conductivity (g) and Seebeck coefficient (h) of layered 2H–$NbSe_2$ and 2H–3R–$NbSe_2$ at 300 K.

band structure using the transport properties while excluding unintended band structure variation due to special confinement [32,33]. The thickness of the layered $NbSe_2$ dispersed on the substrates was determined using AFM, followed by typical lithography and metallization processes to fabricate micro-devices for electrical conductivity and Seebeck coefficient measurements (Fig. 4a and d). The measurement errors were mostly smaller than the symbols expressed in the figures, and some observable errors or gate hysteresis were also negligible compared to the overall variation of transport properties.

The temperature dependence of the electrical conductivity in 2H–$NbSe_2$ exhibited metallic behavior as reported in previous studies and increased with decreasing temperature (Fig. 4b) [18,24,34,35]. Moreover, the change in electrical conductivity caused by the charge density variation in the gate sweep is barely observable, compared to that of the temperature dependence. These metallic characteristics indicate a highly degenerate band structure, which is in a good agreement with that in previous studies on 2H–$NbSe_2$ [16,18,26,27]. In the same manner, the small absolute values of Seebeck coefficient obtained in the 2H sample and their negligible gate dependence can be understood, and the mostly negative values reveal that the major carriers are electrons (Fig. 4c).

Conversely, our 2H–3R–$NbSe_2$ clearly shows gate-dependent transport behavior with noticeable variation, compared to temperature dependence. The electrical conductivity of the 2H–3R sample increased as the gate voltage increased above 0 V and decreased below −10 V (Fig. 4e). Considering that the positive and negative slopes of gate-dependent electrical conductivity reflect electron and hole dominant transport, respectively, the u-shape non-monotonical variation without a steep drop in conductivity reveals the semimetallic band structure. The temperature dependence and low values of electrical conductivity are also consistent with the semimetallic transport. The gate-dependent Seebeck coefficient clearly shows the semimetallic characteristics (Fig. 4f). As the conduction and valence bands overlap, the Seebeck coefficient is determined by the contribution of the major and minor carriers and varies continuously from positive to negative with increasing gate voltage [32]. The maximized absolute values of the Seebeck coefficient are significantly larger than those of the metallic sample because of the semimetallic band structure. We also observed the semimetallic transport behavior in thinner layered 2H–3R–$NbSe_2$ (5.6 nm) (Fig. S3).

These changes in transport properties can be quantitatively evaluated through a comparison of normalized data using zero-gate values

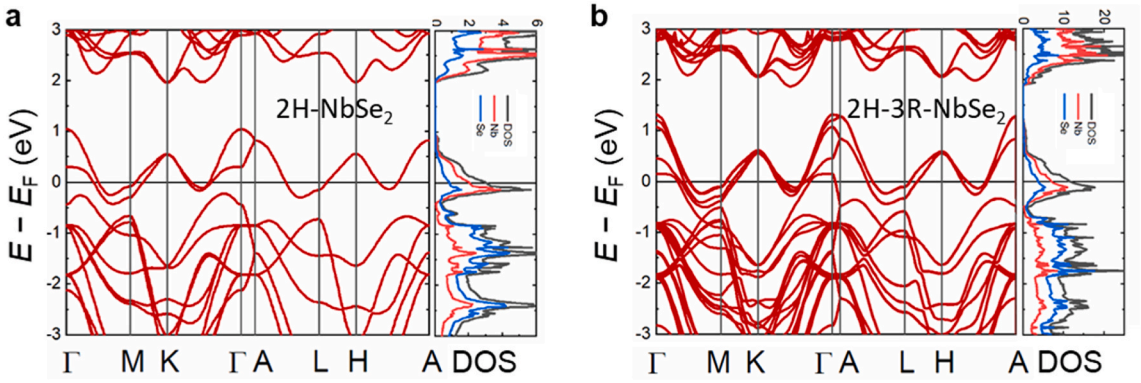

Fig. 5. Theoretical calculations. Electronic band structures and DOS of (a) 2H–$NbSe_2$ and (b) 2H–3R–$NbSe_2$.

(Fig. 4g and h). In the gate sweep from −80 to 80 V, the variations of electrical conductivity and Seebeck coefficient of 2H–3R–$NbSe_2$ are about two and four orders of magnitude larger than those of 2H–$NbSe_2$, respectively. This evidently different transport behavior of our 2H–3R–$NbSe_2$ demonstrates the transition of band structure and the presence of hole carriers due to the differences in the stacking pattern, compared to the 2H–$NbSe_2$ sample.

3.4. *Theoretical calculations*

Finally, to evaluate the change of electronic band structure caused by the difference in the stacking pattern and to verify the observed transport properties, we have conducted first-principle calculations with DFT based on the structural parameters obtained from the TEM analysis (Fig. 5). For 2H–$NbSe_2$, the conduction band structure crossing the Fermi energy (E_F) clearly shows the metallic nature, which is consistent with previous studies and our experimental observation (Fig. 5a) [18,24,34–37]. In 2H–3R–$NbSe_2$, the conduction band structure is similar to that of 2H–$NbSe_2$, except for the split of bands originating from the complex structure of the 2H and 3R combination (Fig. 5b) [38]. However, the valence bands crossing the Fermi energy, observed in the 2H–3R band structure, demonstrate the existence of holes as minor carriers and elucidate the semimetallic features of 2H–3R–$NbSe_2$ observed in the gate-dependent Seebeck coefficient. In particular, transport properties with opposite signs for the electrons and holes (such as the Seebeck coefficient) are very sensitive to the presence of minor carriers, which causes significant changes in the properties as observed between 2H–3R–$NbSe_2$ and 2H–$NbSe_2$ [39].

4. Conclusion

In this study, we systematically investigated the crystal structure and electrical transport properties of the two polymorphs of $NbSe_2$, that is, 2H and 2H–3R. The well-known 2H–$NbSe_2$ shows a typical metallic transport behavior in gate modulation of the electrical conductivity and Seebeck coefficient. However, in the polymorphic form of 2H–3R–$NbSe_2$, significant gate dependencies, which were never observed in the 2H structure, are demonstrated in the electrical conductivity and Seebeck coefficient. This observation clearly indicates that 2H–3R–$NbSe_2$ has a semimetallic feature and the theoretically obtained band structures show the presence of minor carriers in the polymorphic structure. We believe that our findings establish semimetallic 2D $NbSe_2$ as a promising platform to explore polytypic disorder and extend the scope of both the fundamentals and applications of polymorphism in 2D materials.

CRediT authorship contribution statement

Hongjae Moon: Conceptualization, Investigation, Writing - original draft. **Jeongmin Kim:** Methodology, Investigation, Writing - review & editing. **Joonho Bang:** Formal analysis. **Seokkyoon Hong:** Formal analysis. **Seonhye Youn:** Formal analysis. **Hyunjun Shin:** Formal analysis. **Jong Wook Roh:** Resources, Formal analysis. **Wooyoung Shim:** Conceptualization. **Wooyoung Lee:** Supervision, Writing - review & editing.

Declaration of competing interest

The authors declare that they have no known competing financial interests or personal relationships that could have appeared to influence the work reported in this paper.

Acknowledgements

This work was supported by the Agency for Defense Development Republic of Korea (UD170089GD) and the Priority Research Centers Program through the National Research Foundation of Korea (NRF) (2019R1A6A1A11055660). J.K. also acknowledges supports from the DGIST R&D Program (20-ET-07) and Basic Science Research Program (NRF-2019R1I1A1A01063687).

Appendix A. Supplementary data

Supplementary data to this article can be found online at https://doi.org/10.1016/j.nanoen.2020.105197.

References

[1] K. Hantanasirisakul, Y. Gogotsi, Adv. Mater. 30 (52) (2018), e1804779.
[2] J. Zhou, J. Lin, X. Huang, Y. Zhou, Y. Chen, J. Xia, H. Wang, Y. Xie, H. Yu, J. Lei, D. Wu, F. Liu, Q. Fu, Q. Zeng, C.H. Hsu, C. Yang, L. Lu, T. Yu, Z. Shen, H. Lin, B. I. Yakobson, Q. Liu, K. Suenaga, G. Liu, Z. Liu, Nature 556 (7701) (2018) 355–359.
[3] J. You, M.D. Hossain, Z. Luo, Nano Converg. 5 (1) (2018) 26.
[4] J.H. Kim, T.V. Pham, J.H. Hwang, C.S. Kim, M.J. Kim, Nano Converg. 5 (1) (2018) 17.
[5] N. Mounet, M. Gibertini, P. Schwaller, D. Campi, A. Merkys, A. Marrazzo, T. Sohier, I.E. Castelli, A. Cepellotti, G. Pizzi, N. Marzari, Nat. Nanotechnol. 13 (3) (2018) 246–252.
[6] J. Suh, T.L. Tan, W. Zhao, J. Park, D.Y. Lin, T.E. Park, J. Kim, C. Jin, N. Saigal, S. Ghosh, Z.M. Wong, Y. Chen, F. Wang, W. Walukiewicz, G. Eda, J. Wu, Nat. Commun. 9 (1) (2018) 199.
[7] J.A. Wilson, A.D. Yoffe, Adv. Phys. 18 (73) (1969) 193–335.
[8] R. Akashi, M. Ochi, S. Bordács, R. Suzuki, Y. Tokura, Y. Iwasa, R. Arita, Phys. Rev. Appl. 4 (1) (2015).
[9] R. Suzuki, M. Sakano, Y.J. Zhang, R. Akashi, D. Morikawa, A. Harasawa, K. Yaji, K. Kuroda, K. Miyamoto, T. Okuda, K. Ishizaka, R. Arita, Y. Iwasa, Nat. Nanotechnol. 9 (8) (2014) 611–617.
[10] J. Park, I.W. Yeu, G. Han, C.S. Hwang, J.H. Choi, Sci. Rep. 9 (1) (2019) 14919.
[11] D.-S. Kim, H. Kwon, A.Y. Nikitin, S. Ahn, L. Martín-Moreno, F.J. García-Vidal, S. Ryu, H. Min, Z.H. Kim, ACS Nano 9 (7) (2015) 6765–6773.
[12] W. Bao, L. Jing, J. Velasco, Y. Lee, G. Liu, D. Tran, B. Standley, M. Aykol, S. B. Cronin, D. Smirnov, M. Koshino, E. McCann, M. Bockrath, C.N. Lau, Nat. Phys. 7 (12) (2011) 948–952.

[13] T. Taychatanapat, K. Watanabe, T. Taniguchi, P. Jarillo-Herrero, Nat. Phys. 7 (8) (2011) 621–625.
[14] M. Koshino, E. McCann, Phys. Rev. B 80 (16) (2009).
[15] J.M. Lopes Dos Santos, N.M. Peres, A.H. Castro Neto, Phys. Rev. Lett. 99 (25) (2007) 256802.
[16] J.D. Sanchez-Yamagishi, J.Y. Luo, A.F. Young, B.M. Hunt, K. Watanabe, T. Taniguchi, R.C. Ashoori, P. Jarillo-Herrero, Nat. Nanotechnol. 12 (2) (2017) 118–122.
[17] G. Li, A. Luican, J.M.B. Lopes dos Santos, A.H. Castro Neto, A. Reina, J. Kong, E. Y. Andrei, Nat. Phys. 6 (2) (2009) 109–113.
[18] X. Xi, L. Zhao, Z. Wang, H. Berger, L. Forró, J. Shan, K.F. Mak, Nat. Nanotechnol. 10 (9) (2015) 765–769.
[19] G. Kresse, J. Furthmüller, Phys. Rev. B 54 (16) (1996) 11169–11186.
[20] P.E. Blochl, Phys. Rev. B Condens. Matter 50 (24) (1994) 17953–17979.
[21] J.P. Perdew, K. Burke, M. Ernzerhof, Phys. Rev. Lett. 77 (18) (1996) 3865–3868.
[22] S. Grimme, J. Antony, S. Ehrlich, H. Krieg, J. Chem. Phys. 132 (15) (2010) 154104.
[23] S. Grimme, S. Ehrlich, L. Goerigk, J. Comput. Chem. 32 (7) (2011) 1456–1465.
[24] S. Naik, G.K. Pradhan, S.G. Bhat, B.C. Behera, P.S.A. Kumar, S.L. Samal, D. Samal, Physica C: Supercond. Appl. 561 (2019) 18–23.
[25] H. Wang, X. Huang, J. Lin, J. Cui, Y. Chen, C. Zhu, F. Liu, Q. Zeng, J. Zhou, P. Yu, X. Wang, H. He, S.H. Tsang, W. Gao, K. Suenaga, F. Ma, C. Yang, L. Lu, T. Yu, E.H. T. Teo, G. Liu, Z. Liu, Nat. Commun. 8 (1) (2017) 394.
[26] E. Hitz, J. Wan, A. Patel, Y. Xu, L. Meshi, J. Dai, Y. Chen, A. Lu, A.V. Davydov, L. Hu, ACS Appl. Mater. Interfaces 8 (18) (2016) 11390–11395.
[27] C.M. Pereira, W.Y. Liang, J. Phys. C Solid State Phys. 18 (32) (1985) 6075–6082.
[28] J. Yan, J. Xia, X. Wang, L. Liu, J.L. Kuo, B.K. Tay, S. Chen, W. Zhou, Z. Liu, Z. X. Shen, Nano Lett. 15 (12) (2015) 8155–8161.
[29] H. Lin, Q. Zhu, D. Shu, D. Lin, J. Xu, X. Huang, W. Shi, X. Xi, J. Wang, L. Gao, Nat. Mater. 18 (6) (2019) 602–607.
[30] N.D. Boscher, C.J. Carmalt, I.P. Parkin, Eur. J. Inorg. Chem. 6 (2006) 1255–1259, 2006.
[31] J. Heremans, C.M. Thrush, Phys. Rev. B 59 (19) (1999) 12579–12583.
[32] H. Moon, J. Bang, S. Hong, G. Kim, J.W. Roh, J. Kim, W. Lee, ACS Nano 13 (11) (2019) 13317–13324.
[33] A. Ciarrocchi, A. Avsar, D. Ovchinnikov, A. Kis, Nat. Commun. 9 (1) (2018) 919.
[34] H. Luo, J. Strychalska-Nowak, J. Li, J. Tao, T. Klimczuk, R.J. Cava, Chem. Mater. 29 (8) (2017) 3704–3712.
[35] X. Xi, Z. Wang, W. Zhao, J.-H. Park, K.T. Law, H. Berger, L. Forró, J. Shan, K. F. Mak, Nat. Phys. 12 (2) (2015) 139–143.
[36] J.Á. Silva-Guillén, P. Ordejón, F. Guinea, E. Canadell, 2D Mater. 3 (3) (2016).
[37] S. Kim, Y.-W. Son, Phys. Rev. B 96 (15) (2017) 155439.
[38] X. Fan, W.T. Zheng, J.L. Kuo, D.J. Singh, C.Q. Sun, W. Zhu, Sci. Rep. 6 (2016) 24140.
[39] J. Kim, S. Lee, Y.M. Brovman, P. Kim, W. Lee, Nanoscale 7 (2015) 5053–5059.

Hongjae Moon received a Bachelor's degree in Materials Science and Engineering from Yonsei University in 2012. He is currently a Ph.D. candidate at the Department of Materials Science and Engineering in Yonsei University under the supervision of Prof. Wooyoung Lee. He is currently studying on the thermoelectric transport properties of low-dimensional materials.

Jeongmin Kim is a Senior Researcher of the Division of Nanotechnology at DGIST in Korea. He obtained his B.S. degree in metallurgical engineering from Yonsei University in Korea. After his Ph.D. degree in Material Science and Engineering at Yonsei University, he worked as a postdoctoral researcher at UC San Diego and research Professor at Yonsei University. Throughout this time, his prime focus of research has been on studying and enhancing the thermoelectric performance of 1D and 2D materials based on energy band engineering.

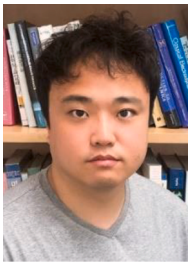

Joonho Bang is currently a research professor in the Department of Energy Science, Sungkyunkwan University, South Korea. He received his Ph.D. in Materials Science and Engineering from the Tokyo Institute of Technology, where he studied strongly correlated systems and amorphous semiconductors. He then worked at the Materials Research Center for Element Strategy, Tokyo Institute of Technology as a specially-appointed assistant professor. His research interests focus mainly on quantum materials and wide-gap semiconductors.

Seokkyoon Hong received a Bachelor's degree in Materials Science and Engineering from Korea University in 2015, and Master's degree in Materials Science and Engineering from KAIST (Korea Advanced Institute of Science and Technology) in 2017. He joined Yonsei University as a researcher in 2018. His current research focuses on the development of thermoelectric nanomaterials.

Seonhye Youn received a Bachelor's degree in chemical Engineering from Kongju National University in 2016. she is currently M.S candidate at the Department of Materials Science and Engineering in Yonsei University under the supervision of Prof. Wooyoung Lee. She is currently studying on the nano thermoelectric materials.

Hyunjun Shin received a Bachelor's degree in Physics and Mathematics from Sogang University in 2015, and Master's degree in Physics from Yonsei University in 2018. Since 2018, he has been in Ph.D. candidate in Physics at Yonsei University, and is working on developing thermoelectric materials as a researcher at the Nano Science Technology Institute at Yonsei University.

Jong Wook Roh have worked as an assistant professor at Kyungpook National University, South Korea from 2018. He obtained his PhD from Yonsei University in 2011, under the supervision of Professor Wooyoung Lee. After graduation, he researched on the low dimensional thermoelectric materials and transparent conduction electrodes materials at Samsung Advanced Institute of Technology from 2011 to 2018. His research focuses on the synthesis and characterization of nanomaterials, especially 1D and 2D materials.

Wooyoung Shim is an associate professor at Yonsei University in Korea. He attended the Yonsei University for his undergraduate education and graduate program for his master degree in the Department of Materials Science and Engineering. After his doctoral studies at the Northwestern University and postdoctoral research at the Harvard University, he moved back to Yonsei in 2014 to assume the position of assistant Professor. At Yonsei, he has been interested in the synthesis of a broad range of nanoscale materials and the development of methods of hierarchical assembly of nanoscale materials, together with the development of nanolithographic tools for future nanotechnology-enabled sensors and related nanoelectronics.

Wooyoung Lee is a professor of the Department of Materials Science and Engineering at Yonsei University in Korea. He received a Ph.D. degree in Physics from University of Cambridge, United Kingdom in 2000. He joined Yonsei University 2003 as professor of Materials Science and Engineering. He is a regular member of National Academy of Engineering of Korea. In recent years, his research interests have centered on thermoelectric materials and devices, permanent magnets, smart gas sensors and breath analyzers. He has received a number of awards in nano-related research areas and a Service Merit Medal (2008) from the Government of Korea due to contribution on the development of intellectual properties. He has authored and co-authored over 200 publications, and has edited three special books on nano-structured materials and devices.